



Feasibility study of using microfluidic platforms for visualizing bubble flows in electrolyzer gas diffusion layers



F. Arbabi^a, A. Kalantarian^{a,b}, R. Abouatallah^c, R. Wang^c, J.S. Wallace^b, A. Bazylak^{a,*}

^aThermofluids for Energy and Advanced Materials (TEAM) Laboratory, Department of Mechanical & Industrial Engineering, Faculty of Applied Science & Engineering, University of Toronto, 5 King's College Road, Toronto, ON M5S 3G8, Canada

^bEngine Research and Development Laboratory (ERDL), Department of Mechanical & Industrial Engineering, Faculty of Applied Science & Engineering, University of Toronto, 5 King's College Road, Toronto, ON M5S 3G8, Canada

^cHydrogenics Corporation, 220 Admiral Boulevard, Mississauga, ON L5T 2N6, Canada

HIGHLIGHTS

- Microfluidic platforms provide means to evaluate PEM electrolyzer GDLs.
- Experimental visualizations of two-phase flow in simulated GDL materials.
- Simulated GDL material properties extracted from computed tomography visualizations.

ARTICLE INFO

Article history:

Received 25 November 2013

Received in revised form

2 February 2014

Accepted 7 February 2014

Available online 19 February 2014

Keywords:

PEM electrolyzer

Bubble visualizations

Microfluidic network

GDL

Porosity distribution

ABSTRACT

In this study, microfluidic platforms were used to visualize air bubble transport in two-dimensional (2D) representations of gas diffusion layers (GDLs) to gain insight into how the geometric features of the GDL impact multiphase flow in polymer electrolyte membrane (PEM) electrolyzers. Two-dimensional porous networks were designed using volumetric pore space information, including average porosity and average throat size obtained from micro-computed tomography (micro CT) visualizations. Microfluidic chips were fabricated to represent felt, sintered powder, and foam GDLs and used to simulate the transfer of oxygen bubbles generated at the catalyst layer, through the GDL towards the flow channels of a PEM electrolyzer. The results of this work indicate that the use of microfluidic platforms for evaluating PEM electrolyzer GDLs is highly promising.

© 2014 Elsevier B.V. All rights reserved.

1. Introduction

The polymer electrolyte membrane (PEM) electrolyzer is a promising technology for producing hydrogen with higher purity and at higher pressure, compared to the competing alkaline electrolyzer [1–5]. Despite a significant increase in PEM electrolyzer research in recent years, there are few studies concerning transport phenomena [6,7]. In particular, the two-phase transport in the gas diffusion layer (GDL) of PEM electrolyzers has only recently been studied by Selamet et al. [6]. They investigated the two-phase flow in the GDL of a PEM electrolyzer by simultaneously using neutron

radiography and optical imaging. They used a fine titanium mesh as the GDL, and they found that the water distribution was influenced by gravity and buoyancy forces. The authors also observed that oxygen gas saturation increased with increasing operating temperature.

Ito et al. [8] experimentally studied the effect of GDL pore properties, such as porosity and pore diameter on PEM electrolyzer performance. They observed that the electrolysis performance improved with decreasing pore diameter, while changes in porosity did not significantly affect the cell performance. Their experimental results showed that larger pores generated larger air bubbles that tended to block the water channels. This group also studied the effect of anode GDL properties on electrolysis by using titanium (Ti)-felt materials with various porosities and pore diameters [9]. Their results showed that gas bubbles hindered the water supply to the electrode, leading to increased concentration overpotentials. For small mean pore diameters the effect of decreasing the water

* Corresponding author. Tel.: +1 (416) 946 5031; fax: +1 (416) 978 7753.

E-mail addresses: arbabi@mie.utoronto.ca (F. Arbabi), kalantar@mie.utoronto.ca (A. Kalantarian), rabouatallah@hydrogenics.com (R. Abouatallah), rwang@hydrogenics.com (R. Wang), wallace@mie.utoronto.ca (J.S. Wallace), abazylak@mie.utoronto.ca (A. Bazylak).

supply on performance was limited, while concentration overpotential increased with increasing mean pore diameter of the anode GDL. Furthermore, they concluded that providing a uniform and suitable contact between the GDL and the catalyst layer reduced not only the contact resistance but also the activation overpotential. While these promising works have been valuable for the development of PEM electrolyzers, further research into the optimization of PEM electrolyzer GDLs is needed for increased efficiency and decreased hydrogen cost.

Direct visualization of two-phase transport in three-dimensional porous media such as the GDL can be challenging due to the opacity of the material [10]. One approach is to visualize two-phase flow in porous networks using microfluidic platforms [11–14], where a 2D representation of a porous media is used for simulating multi-phase flows. Using 2D porous networks to represent 3D porous media is widely used for investigating multi-phase flows in areas such as oil and gas transfer in reservoir rocks [12,14–19] and water management in fuel cell GDLs [20–22]. Berejnov et al. [23] prototyped microfluidic networks and performed fluorescence based visualization to study multiphase transport phenomena in porous media. The authors demonstrated that wettability had a more significant influence on the saturation pattern than pore size distribution. Baouab et al. [14] studied the displacement of air injected into a porous medium saturated with oil and examined the effects of air and oil flow rates and oil viscosity on the displacement of oil. They found that at high oil flow rates and viscosities, air bubbles tended to break apart into smaller bubbles.

Typically, studies such as those described above concerning multi-phase flow in microfluidic chips did not employ pore networks with characteristics obtained directly from porous samples. Pore networks can be obtained from the analysis of high-resolution images [24]. Imaging porous media can be performed in a number of ways, such as micro CT [25–27], focused ion beam-scanning electron microscope (FIB-SEM) [12,25–27], and nuclear magnetic resonance (NMR) imaging [28,29]. Once the 3D reconstructed pore space of a porous medium is captured, the network of pores and throats and their geometrical information can be extracted using numerical methods such as a maximal ball algorithm [30,31], a medial axis algorithm [27,32,33], or a watershed algorithm [24,34]. Recently, Gunda et al. [12] performed water-flooding experiments by designing a microfluidic chip mimicking the porous structure of an oil reservoir rock. They used FIB-SEM to image the rock. Using reconstructed 3D images, the map of pores and throats were extracted. A 2D cross section of the 3D pore network was used to fabricate a 2D network on a microfluidic chip.

One challenging issue in PEM electrolyzers is the coverage of the catalyst layer by oxygen bubbles at the anode, which can hinder the transport of liquid water from the flow fields to the catalyst layer [9]. This mass transport limitation can lead to a decrease in the rate of hydrogen production. It is essential to employ a gas diffusion layer to facilitate the detachment of oxygen bubbles from the catalyst layer in order to reduce gas blockage and enhance the performance of PEM electrolyzers.

In this work, microfluidic platforms were designed and fabricated for the visualization of bubble transport in two-dimensional (2D) representations of three GDLs; felt, sintered powder, and foam. These 2D networks were constructed based on 3D micro-CT reconstructions, and were used to observe the growth, detachment, and propagation of air bubbles in a water-saturated porous medium and to determine the influence of the geometrical properties of the medium on bubble transport behavior. The microfluidic based investigations can be used to inform the design of new GDLs in order to improve electrolyzer efficiency.

There is a high potential for using microfluidic platforms to visualize and investigate two-phase transport in the GDL of PEM electrolyzers. To the best of our knowledge, this is the first use of microfluidic platforms for evaluating PEM electrolyzer GDLs.

2. Methodology

Micro CT technology was employed to image the GDL pore structure. Using a pore space extraction algorithm [24], the pore space information, namely porosity and throat size distributions, was extracted. This information was used to generate representative 2D networks and fabricate microfluidic chips.

Fig. 1 is a schematic of the microfluidic chip, which was used to simulate the two-phase flow of air and water in a PEM electrolyzer. The 2D porous medium was generated based on three-dimensional (3D) volumetric pore space information obtained from microscale computed tomography (micro CT) combined with image processing and pore extraction algorithms developed in-house. The volumetric pore space information obtained from micro CT imaging includes through-plane (across thickness of the material) porosity distributions and throat size distributions for each of the three GDLs. Our methods of micro CT imaging, calculating pore space information, generating representative networks, designing and fabricating microfluidic chips, and visualizing experiments are discussed in detail below.

2.1. Micro CT

Micro CT scans of three GDLs were obtained using SkyScan 1172 (a high-resolution micro-CT scanner; Bruker-micro CT, Belgium). A voltage of 100 kV and a current of 100 μ A were used. A copper filter for removing low energy X-rays (noise) was used to improve the contrast between the titanium sample and the background. A sample size of approximately 6 mm \times 3 mm was scanned for each of the GDLs. The height of the sample was limited by sample holder height (6 mm). It was also found that for a width greater than 3 mm, the noise level of the CT scan became prohibitive. The sample size used here was 18 times larger than the minimum sample size of 1 mm \times 1 mm, recommended by Ref. [35] to obtain a repeatable porosity distribution. The pixel resolution was 2.88 μ m per pixel.

The CT scans were reconstructed using NRECON software (SkyScan). Fiji (image processing software) [36], was then used to reslice the reconstructed greyscale images from the CT scan, in order to visualize the GDL from orthogonal through-plane and in-plane directions. Fig. 2 shows an example of a 3D image of the felt GDL.

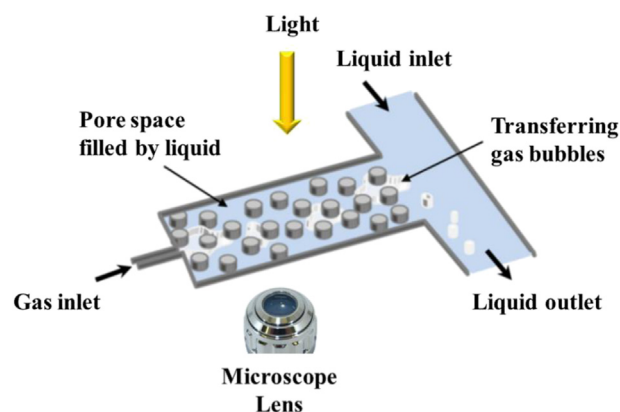


Fig. 1. Schematic of the microfluidic chip for bubble transport visualization. (Figure in colour available online.)

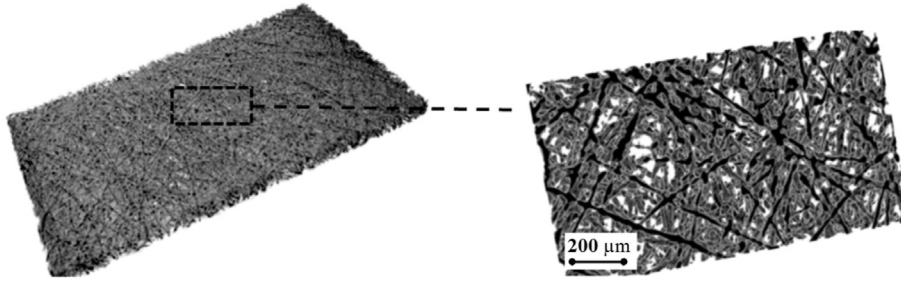


Fig. 2. Micro CT images: 3D image of the felt GDL (left), and enlarged GDL section (right).

2.2. Porosity calculations

In order to generate representative 2D networks, the porosity of the networks was prescribed to be equivalent to the average porosity of the imaged GDLs. This average porosity was calculated using the reconstructed 3D GDL image, which was binarized using Otsu's method [37]. In the binary image, the void space and material were represented by black (0) and white (1), respectively. Fig. 3 shows a sample of an in-plane image of the felt GDL before and after binarization. The local porosity (ϵ) of each in-plane slice is defined as:

$$\epsilon = 1 - \frac{\text{Material pixels}}{\text{Total GDL pixels}} \quad (1)$$

The average porosity for the entire 6 mm × 3 mm samples of felt, sintered powder, and foam was determined with this method to be 68%, 54%, and 77%, respectively.

2.3. Pore network extraction

The void space of any porous medium can be approximated with a network of spherical pores connected with cylindrical throats [12,24]. In this work, the equivalent pore and throat network of GDL samples was extracted using 3D reconstructed CT images. The extracted pore and throat network was then used to generate representative 2D porous networks required for microfluidic chip fabrication (see Section 2.4).

An enhanced watershed algorithm, first implemented in Ref. [24], was used to analyze and extract the equivalent pore and throat network of each GDL type. The input to the algorithm was the binarized stack of in-plane slices obtained in the previous section (Section 2.2). The output is a list of pores, with attributes of location, diameter, and volume, as well as a list of throats, with attributes of diameter and connecting pores. The average pore diameter of the felt, sintered powder, and foam was calculated as 33 μm, 23 μm, and 62 μm, respectively. The average throat diameter of the felt, sintered powder, and foam was calculated as 22 μm, 17 μm, and

45 μm, respectively. The average pore diameter and throat diameter were used to generate the representative 2D porous networks.

The felt GDL consists of cylindrical fibers. Therefore, the cross section of the felt GDL across the length of this layer (through-plane slices) can be approximately simulated as a rectangular domain that consists of solid circles, i.e. 2D representations of fibers.

Our first strategy to generate the 2D network was to match three geometrical properties, i.e. average porosity, average throat diameter, and average pore diameter of the generated 2D networks with the geometrical properties of the actual GDL sample. However, observations obtained from early stage experiments revealed that the air transport in the 2D network was capillary-dominated (see Section 4), whereby the throat diameter dominates the air transport in the saturated porous media, rather than the pore diameter [16]. Therefore, the strategy to generate the 2D network was to match two geometrical properties: the average porosity and average throat diameter of the generated 2D networks, with the corresponding properties of the GDL sample.

The 2D stochastic domain generation algorithm from Ref. [38] was used to generate the 2D networks. The inputs to the algorithm included the network domain size (width and length), porosity, and circle radius. The measured thickness of felt, sintered powder, and foam GDLs were 250 μm, 300 μm, and 750 μm, respectively. Based on the area of the 2D network and the required porosity value, the total area of the solid, i.e. total area of the circles, was calculated. In order to achieve both the desired porosity and average throat radius, both the number and size of circles was considered.

The width of the chip (representing GDL thickness) affects the equivalent throat radius, r_f , of the fabricated network [16], which was calculated as follows:

$$\frac{1}{r_f} = \frac{1}{r_{2D}} + \frac{1}{z} \quad (2)$$

where r_{2D} is the initial throat radius from the generated 2D network, and z is the width of the chip.

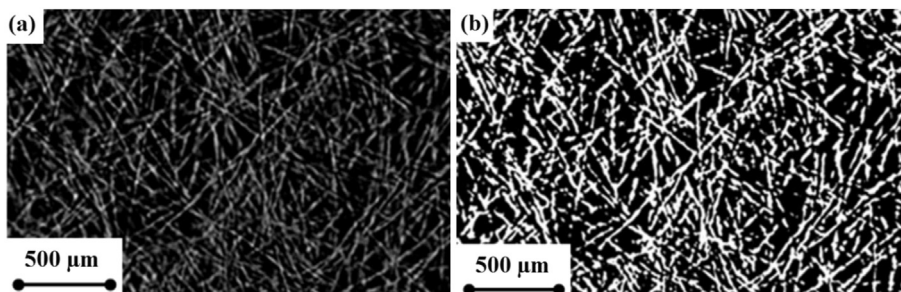


Fig. 3. Example of an in-plane image of the felt GDL before (a) and after binarization (b). The fibers are shown in white.

It was mentioned that the average throat diameter of the felt, sintered powder, and foam was calculated as 22 μm , 17 μm , and 45 μm , respectively. However, generating microfluidic networks for the felt and the sintered powder GDLs with such small throat radii was not feasible, due to the minimum 40 μm clearance between each pair of circles required in the fabrication procedure. Therefore, the average throat size and network width were scaled-up for all chips. A scaling factor of 5 was based on the sintered powder GDL since it had the smallest throat radius and therefore posed the tightest constraint on microfabrication. A set of 2D networks for a range of scaling factors was generated for the sintered powder, and the average throat radius for each generated network was calculated based on Equation (2). Using a scaling factor of 5, the width of the 2D network for the felt GDL was 1.25 mm, which consisted of only 4 circles across the width of the network. However, in the actual felt GDL, there are approximately 8–9 fibers that span across the thickness of the GDL. In order to simulate the GDL more accurately, the width of all three generated networks were doubled, while the other geometrical properties (average porosity and throat size) were kept constant. The final width for the felt, sintered powder, and foam representing networks was 2.5 mm, 3 mm, and 7.5 mm respectively. It was noted that the length of all 2D networks was chosen as the length of the field of view of the objective lens of the microscope used in the experiments, i.e. 16 mm.

The felt and sintered powder networks were 75 μm in height, while the foam network height was 150 μm . The foam network height was chosen to accommodate the larger pore and throat diameters, compared to the felt and sintered powder networks. Specifically, the height was chosen to ensure that a representative number of pores, at the desired porosity with the desired pore diameter, was obtained in the foam network with a 5:1 scaling factor between the representative chip and the real porous material. The height of the foam network also falls within a typically used range for microfluidic chips [39]. Geometric features of the studied GDL samples and their representative 2D pore networks are shown in Tables 1 and 2, respectively.

2.4. Microfluidic chip design and fabrication

The center coordinates of the circles for each of the three generated 2D network were imported into AutoCAD (Version 2013, Autodesk Inc.) using MATLAB [40]. The liquid channel, the inlet and outlet ports for the liquid, the gas channel, and the inlet port for the gas were then designed and added to the 2D network. Fig. 4 depicts a schematic of the microfluidic chip, which fits onto a 75 mm \times 50 mm area.

The microfluidic chips were fabricated using soft lithography [22]. The generated AutoCAD files were printed by CAD/Art Services Inc. (Oregon, USA). The resulting photomask was used in the fabrication process as is shown in Fig. 5(a). The microfabrication process began with patterning a photoresist resin layer on a 75 \times 50 mm glass slide (Corning Inc.). First, a 75 μm layer of SU8-2025 photoresist (MicroChem) was coated on the glass substrate as the seed layer. The seed layer was then baked, exposed to UV light, and baked a second time. In the next step, a layer of SU8-

Table 2
Geometric features of the representative 2D microfluidic pore networks.

	Felt	Sintered powder	Foam
Circle diameter (μm)	150	250	400
Network height (μm)	75	75	150
Network width (mm)	2.5	3	7.5
Network length (mm)	16	16	16

2050 photoresist (MicroChem) was coated on the seed layer using a spin coater, to achieve the desired thickness (Table 2). The photoresist layer was then soft-baked to evaporate solvent and condense the photoresist. In the next step, the photoresist layer was exposed to a UV light source while the photomask was placed on it (Fig. 5(b)). The exposure step allows for photoresist cross-linkage. The photoresist layer was baked again to complete the photoresist cross-linking reaction. Any SU8-2050 photoresist substrate not exposed to UV light was removed with chemical etching. The result was a patterned template master, as can be seen in Fig. 5(c). The final chip was then fabricated by curing polydimethylsiloxane (PDMS) on the patterned template, shown in Fig. 5(d). The cured PDMS was then peeled off from the master and sealed to a 75 \times 50 mm glass slide using a plasma bonding process (Fig. 5(e)).

2.5. Experimental setup

The visualization of air bubble invasion into the liquid-saturated porous network was performed using fluorescence microscopy. Titanium GDLs are naturally hydrophilic [41]; however, PDMS is naturally hydrophobic. To achieve a similar wettability condition to that of titanium, ethanol was chosen as the wetting liquid, which showed a similar contact angle ($\sim 50^\circ$) on PDMS as the contact angle of water on titanium. The ethanol was tagged with a dilute solution of fluorescein dye (Fluorescent sodium salt, Sigma–Aldrich, 0.001 M) to identify the interface between the liquid and the gaseous air.

An inverted compound microscope (DMI 3000 B, Leica) was used for all visualizations and illuminated from below with a fluorescent light source (X-Cite Series 120 Q, Lumen Dynamics Group Inc.). The experimental setup and the microfluidic chip under the microscope can be seen in Fig. 6. The liquid inlet port was attached to a 1 mL syringe via tubing (Radel brand, ID: 0.02 inch,

Table 1
Geometric features of the GDL samples.

	Felt	Sintered powder	Foam
Porosity (%)	68	54	77
Average pore diameter (μm)	33	23	62
Average throat diameter (μm)	22	17	45
Thickness (μm)	250	300	750

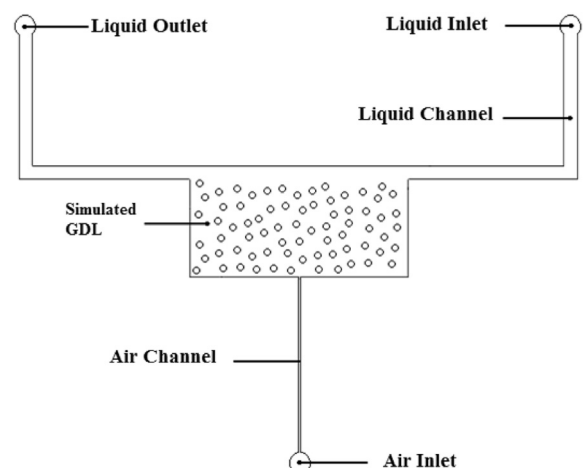


Fig. 4. Schematic of the microfluidic chip designed for the foam GDL.

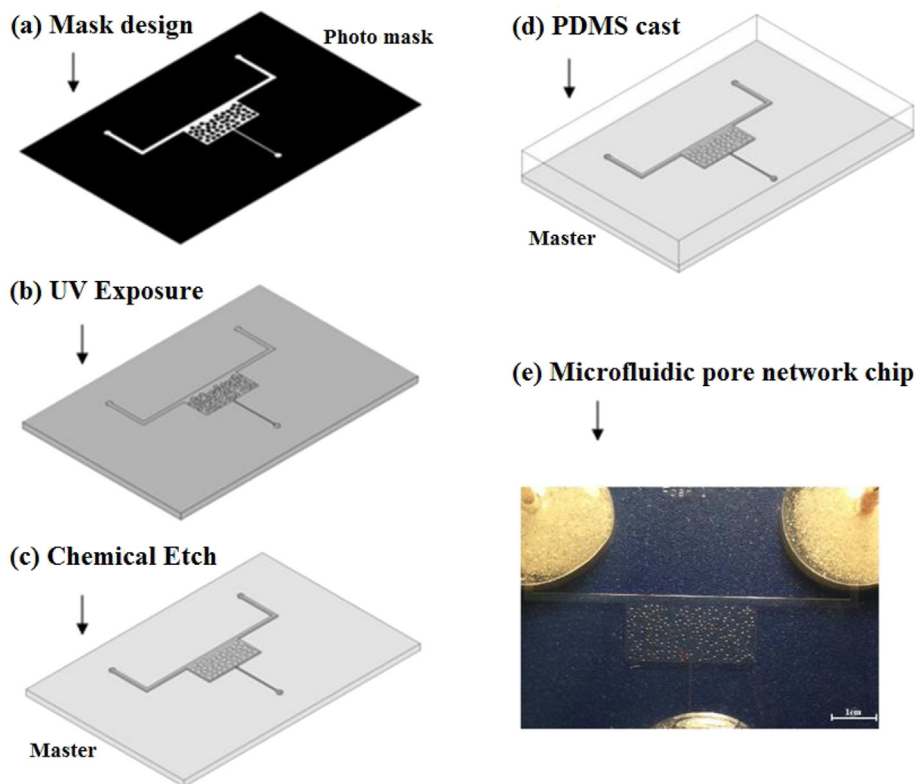


Fig. 5. Fabrication procedure for a microfluidic chip (a) a photomask is produced. (b) A flat substrate coated with a thin photoresist layer is exposed to UV light. (c) Unexposed photoresist is chemically etched away, leaving a planar 3D pore network structure (master). (d) A PDMS elastomeric replica of master is cast. (e) Cured PDMS is bonded to a glass slide to make the microfluidic chip.

Idex Health and Science). The syringe was mounted on a syringe pump (11 plus, Harvard Apparatus) to control the liquid flow rate. The air inlet port was also attached to a 1 mL syringe through tubing, and the syringe was mounted on a syringe pump to control the air flow rate. A CCD camera (pco. 1600 monochrome, PCO, Germany) was connected to the microscope, and image acquisition was performed using Camware software (PCO, Germany). The images were captured at a frame rate of 32.41 fps. The images were in greyscale format with a spatial resolution of 800 pixels \times 600 pixels.

3. Scope of investigation

The air and liquid flow rates were varied to investigate their effects on the air transport behavior in the porous network at room temperature. To estimate the air flow rate, the information provided in Ref. [42] for a Giner GS-10 PEM electrolyzer (Giner Electrochemical Systems LLC, US) was used. The oxygen production rate for the electrolyzer in Ref. [42] was $0.55 \text{ N m}^3 \text{ h}^{-1}$ at 1.4 A cm^{-2} for a stack of 12 planar cells, with an exchange surface of 160 cm^2 . Based on the cross sectional area of the air channel, the equivalent air flow

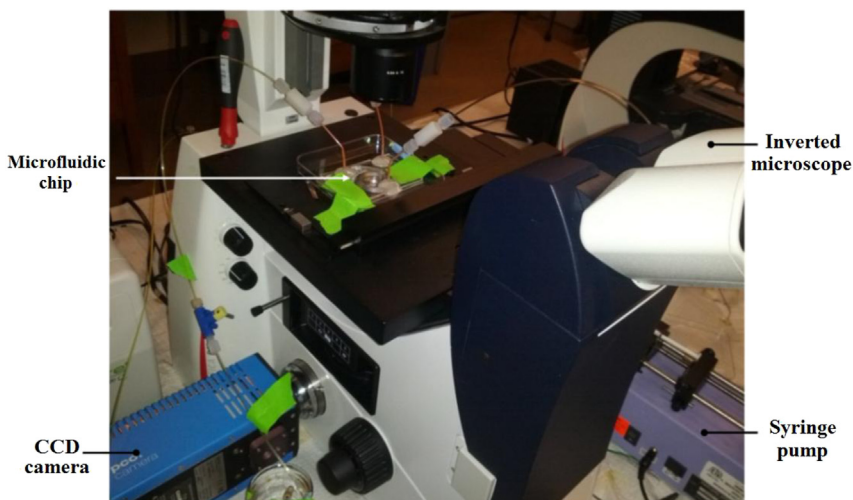


Fig. 6. Experimental setup used for the bubble visualization in the GDL.

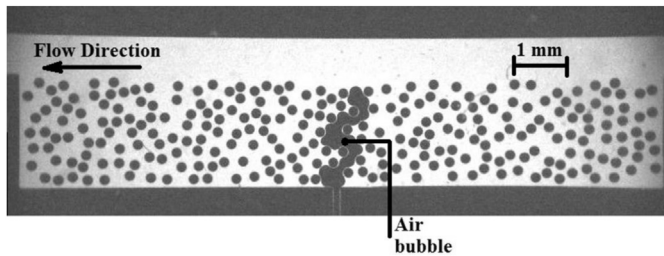


Fig. 7. Greyscale image of the breakthrough moment for the microfluidic chip representing the felt GDL.

rate required for the microfluidic chip was calculated to be approximately $1 \mu\text{L min}^{-1}$. To examine the effect of air flow rate on bubble transport, three air flow rates were used: 1, 5 and $10 \mu\text{L min}^{-1}$ (corresponding to current densities of 1.4, 7.0, and 14 A cm^{-2} , respectively). To the authors' best knowledge, water channel flow rates were not available in the literature; therefore, the water flow rate was chosen to be similar to the air flow rate. In the preliminary experiments, two liquid flow rates were tested: $5 \mu\text{L min}^{-1}$ and $10 \mu\text{L min}^{-1}$. The results showed that changing the liquid flow rate did not affect the pattern of air invasion into the pores of the network or the air breakthrough location. Therefore, only one liquid flow rate ($10 \mu\text{L min}^{-1}$) was used for subsequent investigations. It should be noted that all experiments were conducted at room temperature. Temperature and pressure are expected to have an impact on multiphase transport, and should be studied in future work.

3.1. Procedure

Initially, the liquid flow rate was set to $10 \mu\text{L min}^{-1}$ throughout the experiment. Once, the liquid fully saturated the porous network, the air injection and image acquisition began simultaneously. The imaging continued until the air reached the liquid channel (breakthrough moment), and air bubbles formed and detached in the liquid channel. Once breakthrough occurred, the air injection and imaging ceased. The air injection experiment was repeated for each chip for three air flow rates: 1, 5, and $10 \mu\text{L min}^{-1}$.

4. Results and discussion

The 2D microfluidic pore networks were generated to represent the 3D GDL materials analyzed with the micro CT system, from which we determined that the samples under investigation had porosities of 68%, 54%, and 77% for felt, sintered powder, and foam, respectively. Images captured during air invasion were analyzed with Fiji (image processing software). Figs. 7–9 show greyscale images of three porous networks at breakthrough, i.e. the moment at which a continuous air bubble connects the inlet to the liquid

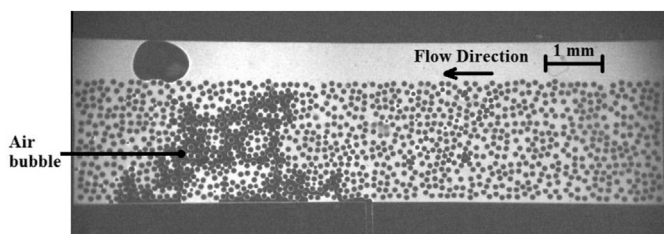


Fig. 8. Greyscale image of the breakthrough moment for the microfluidic chip representing the sintered powder GDL.

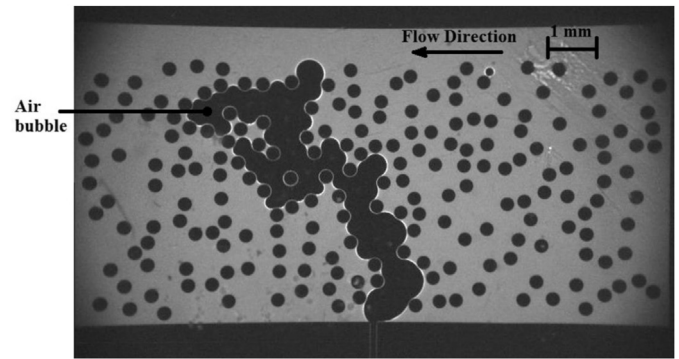


Fig. 9. Greyscale image of the breakthrough moment for the microfluidic chip representing the foam GDL.

channel. The solid structure and the air bubble cluster appear as black, and the liquid appears as white in the images.

A quantitative criterion to compare the three microfluidic chips is to calculate the amount of air trapped in the porous network at the breakthrough moment. Lower saturation values of trapped air are preferable for enhanced liquid water transport to the catalyst layer. First, images were converted to binary images using ImageJ (image processing software) to distinguish the air bubble and the solid structure from the liquid. In the binary images, the air bubble and the solid structure are represented by black (0) and the liquid is represented by white (1) pixels. The number of solid structure pixels was first calculated using an image of the porous network with no air, i.e. before air invasion began. Then, the total number of black pixels (air pixels + solid structure pixels) and the total number of white pixels (liquid pixels) were calculated for each binarized image. By subtracting the number of solid structure pixels from the total number of black pixels, the number of air pixels was calculated for each image. The air saturation (s) for each image is defined as:

$$s = \frac{\text{Air pixels}}{\text{Liquid pixels} + \text{Air pixels}} \quad (3)$$

Equation 3 was applied to each image, and the air saturation was calculated for each image. Fig. 10 shows the air saturation calculated during the invasion process for the three microfluidic chips each representing a GDL material. The air flow rate for Fig. 10 was $1 \mu\text{L min}^{-1}$. The air saturation during the invasion process was also calculated for the other air flow rates (5 and $10 \mu\text{L min}^{-1}$), and it was found that the saturation was independent of air flow rate.

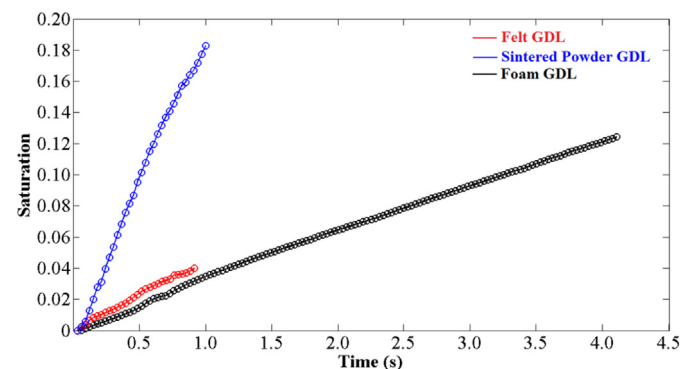


Fig. 10. Saturation profile calculated for the microfluidic chip representing the felt, sintered powder, and foam GDLs. Each data point on the saturation profiles represents an image acquired in the invasion process at the rate of 32.41 fps. (Figure in colour available online.)

Investigating the images taken during the invasion process reveals that air bubble snap-off [43,44] did not occur during the air invasion process, i.e. the advancing air bubble cluster did not break apart into smaller bubbles. In fact, the air remained as a large cluster during the invasion process that sequentially filled the pores until a single, connected exit path to the liquid channel was established.

As mentioned before, changing the air flow rate from 1 to 10 $\mu\text{L min}^{-1}$, i.e. 1.4 A cm^{-2} to 14 A cm^{-2} in electrolyzers, did not affect the breakthrough air flow pattern. Therefore, it can be concluded that air transport in the 2D network remains capillary-dominated even at relatively high air flow rates, i.e. high current densities in electrolyzers.

Comparing the saturation profiles at the breakthrough moment for the three types of microfluidic chips (Fig. 10) reveals that the saturation for the microfluidic chip representing the felt GDL is lower than the other two microfluidic chips. This might imply that for the felt GDL, the relative amount of air occupying the available pore space could be less than that of foam and sintered powder GDLs. Felt may therefore have a lower resistance for water to reach the catalyst layer, possibly resulting in higher PEM electrolyzer efficiency. The networks, such as those shown here, can be used to further investigate the merits of these types of GDLs.

While only three networks have been shown here to demonstrate the feasibility of using microfluidic platforms for visualizing air bubble transport, it is important to note that further experiments involving parametric studies of porosity, particle size and distribution, domain size, etc. will be needed to gain an in-depth understanding of how these parameters affect the bubble transport trends. The capillary-dominated flow patterns in these networks are deterministic, depending on a variety of parameters including domain size [45]. Therefore it is important to note that these results provide useful examples of potential flow patterns and should not be used solely to determine the merits of each GDL. This study will be extended in the future to determine which GDL type is preferable for low air saturations and which parameters dominate the air transport behavior.

5. Conclusions

In this work, the feasibility of using microfluidic platforms for visualizing air bubble transport in PEM electrolyzer GDLs was investigated. Representative 2D networks that simulate the pore network of three types of GDLs, i.e. felt, sintered powder, and foam were designed using volumetric pore space information (average porosity and average throat size) obtained from micro CT images. Using representative 2D networks, three microfluidic chips each representing a GDL were designed and fabricated. The reported method is highly promising for investigating the influence of the geometrical features of the GDL on air transport within the porous medium.

The visualization of air injection into the liquid-saturated porous network of the microfluidic chips showed that the transport mechanism of air bubbles in the GDL is capillary-dominated even at high air flow rates, i.e. high current densities.

Our results showed that the air saturation at the breakthrough moment is smaller for the microfluidic chip representing the felt GDL. However, this preliminary finding does not imply that the felt GDL would be preferable for PEM electrolyzers. A deeper comparison of the three types of GDLs requires more investigation of the effect of the medium's geometric properties, e.g. porous medium thickness, porosity, tortuosity, pore size and throat size, on the bubble transport behavior.

Acknowledgments

The authors would like to gratefully acknowledge the financial support of the Natural Sciences and Engineering Research Council of Canada (NSERC) through the Engage program and the NSERC CREATE Program in Distributed Generation for Remote Communities for their financial support. The authors would also like to gratefully acknowledge the collaborative support and in-kind contributions of their industrial partner, Hydrogenics Corp. Special thanks are also given to Mr. James Hinebaugh, Dr. Ronnie Yip, Dr. Hanif Montazeri, Dr. Jonathan Ellis and Mr. Pradyumna Challa, for their helpful discussions throughout this project. Thanks also to Prof. Mark Kortschot in the Department of Chemical Engineering and Applied Science for providing access to the SkyScan 1172 Micro CT system.

References

- [1] A. Ursua, L.M. Gandia, P. Sanchis, *Proc. IEEE* 100 (2012) 410–426.
- [2] F. Barbir, *PEM Fuel Cells: Theory and Practice*, Academic Press, San Diego, 2005.
- [3] M. Carmo, D.L. Fritz, J. Mergel, D. Stolten, *Int. J. Hydrogen Energy* 38 (2013) 4901–4934.
- [4] T. Smolinka, *Fuels – Hydrogen Production|Water Electrolysis*, in: Editor-in-Chief: G. Jürgen (Ed.), *Encyclopedia of Electrochemical Power Sources*, Elsevier, Amsterdam, 2009, pp. 394–413.
- [5] S.A. Grigoriev, V.I. Porembsky, V.N. Fateev, *Int. J. Hydrogen Energy* 31 (2006) 171–175.
- [6] O.F. Selamet, U. Pasaogullari, D. Spornjak, D.S. Hussey, D.L. Jacobson, M. Mat, *ECS Trans.* 41 (2011) 349–362.
- [7] S. Siracusano, A. Di Blasi, V. Baglio, G. Brunaccini, N. Briguglio, A. Stassi, R. Ornelas, E. Trifoni, V. Antonucci, A.S. Aricò, *Int. J. Hydrogen Energy* 36 (2011) 3333–3339.
- [8] H. Ito, T. Maeda, A. Nakano, C.M. Hwang, M. Ishida, A. Kato, T. Yoshida, *Int. J. Hydrogen Energy* 37 (2012) 7418–7428.
- [9] H. Ito, T. Maeda, A. Nakano, A. Kato, T. Yoshida, *Electrochim. Acta* 100 (2013) 242–248.
- [10] S. Litster, D. Sinton, N. Djilali, *J. Power Sources* 154 (2006) 95–105.
- [11] N.K. Karadimitriou, S.M. Hassanizadeh, *Gsvadzone* 11 (2012).
- [12] N.S. Gunda, B. Bera, N.K. Karadimitriou, S.K. Mitra, S.M. Hassanizadeh, *Lab Chip* 11 (2011) 3785–3792.
- [13] J. Joseph, N. Siva Kumar Gunda, S.K. Mitra, *Chem. Eng. Sci.* 99 (2013) 274–283.
- [14] Z. Baouab, M. Najjari, H. Ouerfelli, S.B. Nasrallah, *J. Petrol. Sci. Eng.* 59 (2007) 250–256.
- [15] R. Fisher, M.K. Shah, D. Eskin, K. Schmidt, A. Singh, S. Molla, F. Mostowfi, *Lab Chip* 13 (2013) 2623–2633.
- [16] C. Cottin, H. Bodiguel, A. Colin, *Phys. Rev. E* 84 (2011) 026311.
- [17] B. Yadali Jamaloei, K. Asghari, R. Kharat, F. Ahmadloo, *J. Petrol. Sci. Eng.* 72 (2010) 251–269.
- [18] N.K. Karadimitriou, V. Joekar-Niasar, S.M. Hassanizadeh, P.J. Kleingeld, L.J. Pyrak-Nolte, *Lab Chip* 12 (2012) 3413–3418.
- [19] M. Sohrabi, A. Danesh, M. Jamiolahmady, *Transp. Porous Med.* 74 (2008) 239–257.
- [20] V. Berejnov, A. Bazylak, D. Sinton, N. Djilali, *J. Electrochem. Soc.* 157 (2010) B760–B767.
- [21] O. Chapuis, M. Prat, M. Quintard, E. Chane-Kane, O. Guillot, N. Mayer, *J. Power Sources* 178 (2008) 258–268.
- [22] A. Bazylak, V. Berejnov, B. Markicevic, D. Sinton, N. Djilali, *Electrochim. Acta* 53 (2008) 7630–7637.
- [23] V. Berejnov, N. Djilali, D. Sinton, *Lab Chip* 8 (2008) 689–693.
- [24] J. Hinebaugh, A. Bazylak, in: *ASME 2012 6th International Conference on Energy Sustainability & 10th Fuel Cell Science, Engineering and Technology Conference*, San Diego, CA, USA, 2012.
- [25] M.J. Blunt, M.D. Jackson, M. Piri, P.H. Valvatne, *Adv. Water Resour.* 25 (2002) 1069–1089.
- [26] M.J. Blunt, *Curr. Opin. Colloid Interface Sci.* 6 (2001) 197–207.
- [27] R.I. Al-Raoush, C.S. Willson, *J. Contam. Hydrology* 77 (2005) 67–89.
- [28] J.D. Seymour, P.T. Callaghan, *AIChE J.* 43 (1997) 2096–2111.
- [29] KENYON, #160, W. E., *Nuclear Magnetic Resonance as a Petrophysical Measurement*, Pergamon Press, Oxford, ROYAUME-UNI, 1992.
- [30] A.S. Al-Kharusi, M.J. Blunt, *J. Petrol. Sci. Eng.* 56 (2007) 219–231.
- [31] H. Dong, M.J. Blunt, *Phys. Rev. E* 80 (2009) 036307.
- [32] W.B. Lindquist, S.-M. Lee, D.A. Coker, K.W. Jones, P. Spanne, *J. Geophys. Res. Solid Earth* 101 (1996) 8297–8310.
- [33] W.B. Lindquist, A. Venkatarangan, *Phys. Chem. Earth, Part A Solid Earth and Geodesy* 24 (1999) 593–599.
- [34] L. Vincent, P. Soille, *IEEE Trans. Pattern Anal. Mach. Intell.* 13 (1991) 583–598.
- [35] Z. Fishman, J. Hinebaugh, A. Bazylak, *J. Electrochem. Soc.* 157 (2010) B1643–B1650.

- [36] J. Schindelin, I. Arganda-Carreras, E. Frise, V. Kaynig, M. Longair, T. Pietzsch, S. Preibisch, C. Rueden, S. Saalfeld, B. Schmid, J.-Y. Tinevez, D.J. White, V. Hartenstein, K. Eliceiri, P. Tomancak, A. Cardona, *Nat. Methods* 9 (2012) 676–682.
- [37] N. Otsu, *IEEE Trans. Systems, Man and Cybernetics* 9 (1979) 62–66.
- [38] J. Hinebaugh, Z. Fishman, A. Bazylak, *J. Electrochem. Soc.* 157 (2010) B1651–B1657.
- [39] Daniel S. Park, Saade Bou- Mikael, Sean King, Karsten E. Thompson, Clinton S. Willson, D.E. Nikitopoulos, in: *ASME 2012 International Mechanical Engineering Congress and Exposition*, Houston, Texas, USA, 2012, pp. 709–715.
- [40] J. Trevelyan, in: <http://school.mech.uwa.edu.au/~jamest/matlab-dxf/>, August 2000.
- [41] Y.J. Lim, Y. Oshida, *Bio-Med. Mater. Eng.* 11 (2001) 325–341.
- [42] M. Santarelli, P. Medina, M. Cali, *Int. J. Hydrogen Energy* 34 (2009) 2519–2530.
- [43] A.R. Kavscek, C.J. Radke, *Colloids Surf. A Physicochem. Eng. Asp.* 117 (1996) 55–76.
- [44] T.M. Tsai, M.J. Miksis, *J. Fluid Mech.* 274 (1994) 197–217.
- [45] R. Lenormand, *Proc. R. Soc. London Math. Phys. Sci.* 423 (1989) 159–168.